

Structural study of bimetallic $\text{Co}_x\text{Rh}_{1-x}$ nanoparticles: Size and composition effects

M. C. Fromen, P. Lecante, and M. J. Casanove*

Centre d'Élaboration de Matériaux et d'Études Structurales, C.N.R.S., 29, Rue Jeanne Marvig, 31055 Toulouse Cedex 4, France

P. Bayle Guillemaud

CEA, Département de Recherche Fondamentale sur la Matière Condensée, SP2M 17, Rue des Martyrs, 38054 Grenoble, France

D. Zitoun, C. Amiens, and B. Chaudret

Laboratoire de Chimie de Coordination, C.N.R.S., 205, route de Narbonne, 31077, Toulouse Cedex 4, France

M. Respaud

Laboratoire de Physique de la Matière Condensée, I.N.S.A., 135 Avenue de Rangueil, 31077 Toulouse Cedex 4, France

R. E. Benfield

Functional Materials Group, School of Physical Sciences, University of Kent, Canterbury, CT2 7NR, United Kingdom

(Received 15 December 2003; published 28 June 2004)

The structure of ultrafine bimetallic $\text{Co}_x\text{Rh}_{1-x}$ nanoparticles synthesized in mild conditions by codecomposition of organometallic precursors in the presence of a polymer or a ligand has been studied using high-resolution electron microscopy and wide-angle x-ray scattering techniques. While pure rhodium particles exhibit the main structural features of a face centered cubic (fcc), alloying with cobalt induces a progressive loss of periodicities, leading in high-cobalt-content particles to a polytetrahedral structure close to the one already encountered in pure-cobalt particles. When increasing the synthesis temperature, the polytetrahedral structure remains remarkably stable, while particles with higher rhodium content clearly evolve towards perfect fcc. Increasing the size of the particles up to 5–6 nm stabilizes the structural phases encountered in the phase diagram of the bulk alloy. Different element-sensitive techniques, x-ray absorption spectroscopy (XANES and EXAFS) and energy-filtering transmission electron microscopy, have also been implemented in order to get chemical information. Evidence is given for a cobalt surface segregation in these bimetallic particles, highly favorable for magnetic-moment enhancement.

DOI: 10.1103/PhysRevB.69.235416

PACS number(s): 61.46.+w, 61.10.Eq, 68.37.Lp, 61.10.Ht

I. INTRODUCTION

Investigations of size effects in nanometer-sized particles have been intensively carried out in the last few years, both in theoretical and in experimental approaches. In particular, evidence has been given of strong size-related magnetic effects in metallic particles. For instance, in a $4d$ metal as rhodium, the occurrence of ferromagnetism in small clusters including less than 50 atoms was both calculated and experimentally demonstrated.^{1,2} Combining size effects and alloying with a $3d$ metal, already known as an effective way to induce spin polarization in $4d$ metals, was recently undertaken in our group.³ In this previous paper, we reported the synthesis and magnetic study of bimetallic $\text{Co}_{0.5}\text{Rh}_{0.5}$ particles with diameters lying in the 1–3 nm range. The synthesis process, already successfully followed for cobalt clusters,^{4,5} was based on the decomposition of organometallic precursors in mild conditions of pressure and temperature in the presence of a polymer, the polyvinylpyrrolidone (PVP). Both the magnetic and the structural results obtained on cobalt particles demonstrated that they behave as free particles, with very weak or none interaction with the PVP polymer. The results obtained on CoRh particles stabilized in PVP also agreed with a good surface state of the particles. The cooperative role of alloying and size reduction was demonstrated through the strong enhancement of the saturation

magnetization in particles with 1.65 nm of mean diameter compared to the predicted value for the bulk alloy.⁶ In parallel, size reduction is also known to influence the structural organization and to exalt the role played by surface segregation in metallic alloys. The first structural investigations, performed by high-resolution transmission electron microscopy (HRTEM) and wide angle x-ray scattering (WAXS), on $\text{Co}_x\text{Rh}_{1-x}$ particles with $0 \leq x \leq 1$ synthesized in PVP gave evidence for two major features.^{7,8} First, the mean metal-metal bond-length (d_{mm}) in the alloyed particles remains close to the pure Rh mean metal-metal distance, whatever the composition, provided some rhodium is introduced. Its value is then systematically higher than the one reported in the bulk alloy of same composition. Secondly, the crystallographic order in the bimetallic CoRh particles tends to improve with increasing Rh content. The structure of pure cobalt particles with same size and synthesized by the same chemical route has already been proposed as a well-defined polytetrahedral arrangement.⁵ Alloying with rhodium, as alloying with platinum that we studied in a previous work,⁹ seems to introduce structural disorder in the Co-rich particles, at least at the surface, which impedes their unambiguous structural determination.

In relation with these first results, we focus in this paper on the structural evolution of $\text{Co}_x\text{Rh}_{1-x}$ particles with $0 \leq x \leq 1$ both with composition and synthesis conditions, likely to

influence the size and the structure of the particles. Particular attention was also paid to the chemical distribution inside the particles. Indeed, the presence of weakly ordered structures in PVP stabilized $\text{Co}_x\text{Rh}_{1-x}$ particles can result from the formation of metastable states at room temperature. Syntheses at higher temperature, 80°C , have then been carried out and we follow the evolution of the structural features for the different compositions. Increasing the size of the particles is also likely to bring elements for solving the $\text{Co}_x\text{Rh}_{1-x}$ particles structure. This size is, however, largely influenced by the nature of the stabilizer. The synthesis of larger particles has then been performed in an organic ligand, the hexadecylamine (HDA). The structure of the different samples is investigated by a combination of HRTEM and WAXS experiments. HRTEM provides direct size estimation, morphology, and spatial distribution of individual particles, as well as structural evidences, mainly through the analysis of lattice periodicities. WAXS provides an accurate set of interatomic distances. This technique, dedicated to amorphous or weakly crystallized materials, is particularly suited for solving non-periodic structures. The chemical distribution inside the particles is analyzed using element-sensitive techniques as extended x-ray absorption fine structure (EXAFS) and energy filtering transmission electron microscopy (EFTEM). The latter technique enables local analyzes on a single particle, at least the larger ones, and thus provides a chemical map of the different species. The former probes the short-range order around a specific element, whatever the particle size. The chemical information is, however, indirectly retrieved from these structural features through numerical refinement of models.

II. SYNTHESIS, STRUCTURAL AND EXPERIMENTAL DETAILS

A. Synthesis

The different $\text{Co}_x\text{Rh}_{1-x}$ samples were all synthesized using a chemical route based on the codecomposition under dihydrogen (3 bars) of two organometallic precursors, namely $\text{Co}(\eta^3\text{-C}_8\text{H}_{13})(\eta^4\text{-C}_8\text{H}_{12})$ and $\text{Rh}(\text{acetylacetonate})(\eta^4\text{-C}_8\text{H}_{12})$, in a solvent containing either a polymer or a ligand. The polymer/solvent couple is PVP/tetrahydrofuran (THF). The toluene was used for the samples in HDA. The final composition of the particles was adjusted by varying the relative initial proportion of the two precursors. Except for the pure Co or Rh particles, three typical compositions were studied in the polymer PVP: $\text{Co}_{0.5}\text{Rh}_{0.5}$, $\text{Co}_{0.25}\text{Rh}_{0.75}$, and $\text{Co}_{0.75}\text{Rh}_{0.25}$, respectively, named in the following Co1Rh1, Co1Rh3, and Co3Rh1. The final compositions, determined by chemical microanalysis, are no more than 2.7% far from the nominal composition. Four different compositions have been studied in HDA (see Table III). A more complete description of the synthesis can be found in Refs. 8 and 10.

B. HRTEM and EFTEM experiments

Specimens for TEM investigations were prepared by slow evaporation of droplets of a solution of the colloid diluted in methanol deposited on high-resolution carbon supported

copper mesh. In order to limit oxidation effects, the deposits were done in an argon atmosphere and the microgrids were kept in this atmosphere until they were placed in the TEM specimen holder. However, during this last step, the grids are still exposed to air for a short time. The HRTEM experiments were performed on a Philips CM30/ST operated at 300 kV, with a point resolution of 0.19 nm. For each sample, a size distribution histogram of at least 200 particles was plotted from the numerical analysis of several micrographs. HRTEM images of isolated particles were recorded at a resolution of 0.03 nm/pix using a Gatan slow-scan charge coupled device (CCD) camera. When present, the lattice periodicities in the particles were analyzed using numerical diffractograms of the image (Fourier transforms). EFTEM experiments were performed on some samples using a JEOL 3010 microscope operated at 300 kV and fitted with a post-column filter (GATAN 200 model). The filtered images were recorded on a CCD camera. A three-window procedure was used to extract the characteristic signal of the cobalt and rhodium edges.¹¹ In this procedure three filtered images were recorded, two before the edge and one after, using the same width for the energy window. The images recorded before the edge allowed us to extrapolate the background to be extracted from the third filtered image. This last one contains the information on the spatial distribution of the analyzed element. Analyses were performed on the Co-L_{23} and the Rh-M_{45} edges with energy window widths of 15 and 10 eV, respectively.

C. WAXS and EXAFS experiments

WAXS experiments were mainly performed at CEMES using a dedicated two-axis diffractometer. Measurements of the intensity scattered by the samples were performed at the molybdenum K_α (0.071069 nm) wavelength. Since only the primary beam was graphite monochromatized, an aluminium filter was inserted in the diffracted beam in order to suppress fluorescence from cobalt. Data typically include 457 measurements in the range $0^\circ \leq \theta \leq 65^\circ$ for equidistant s values [$s = 4\pi(\sin \theta/\lambda)$]. Additional measurements were also performed at the European Synchrotron Radiation Facility (ESRF) in Grenoble (France) on the high-energy diffraction beamline ID15B. The much higher energy available (90 keV) combined to the very high intensity and parallel measurement of all angles using an image plate as detector led to faster measurements (typically 20 min instead of 20 h in laboratory), better statistics and a larger cutoff for s (26 \AA^{-1} vs 17 \AA^{-1} for our diffractometer). The same samples were used for both measurements: small amounts of dry colloidal powder sealed in thin-walled Lindemann glass capillaries of 1.5 mm diameter. The same treatments were applied to all data sets: physical corrections for polarization and self-absorption as well as subtraction of the corrected scattering from glass capillary and PVP. Scattering from the relatively very small amount of ligands surrounding bigger particles could actually be neglected. An additional benefice of the high energy used on ID15B was to greatly reduce absorption effects. Data were normalized to one metal atom, taking into account the mean scattering power for the binary systems.

The so-called reduced intensity function was extracted then Fourier transformed in order to obtain the radial distribution function (RDF). A full description of this procedure can be found in Ref. 12. Analysis of the experimental RDF provides good estimates of the mean metal-metal bond length and the order extent inside the particles, hereafter called the coherence length. In the more favorable situation, the position and relative intensity of the different peaks provide a signature of a single three-dimensional structure. However, in the general case, comparison with computed theoretical RDF, also normalized to one atom, using different models are required. The size of the theoretical model is chosen to reproduce the experimental coherence length, and the cell parameter is contracted or dilated in order to match the experimental first metal-metal bond length. The computed RDF are obtained using the Debye formula

$$i_D(s) = 2 \sum_{i=1}^{N-1} \sum_{j=i+1}^N f_i(s) f_j(s) \frac{\sin(sr_{ij})}{sr_{ij}} \exp(-b_{ij}s^2), \quad (1)$$

where N is the total number of atoms in the model, f_i is the atomic scattering factor for atom i , r_{ij} is the distance between atoms i and j , and b_{ij} is a dispersion factor affecting the i - j interaction.

X-ray absorption (XANES and EXAFS) experiments were performed for some samples on beamline X1 at HASYLAB in Hamburg. The samples were prepared by compacting a pellet of the powder in a polyethylene matrix, in order to have a higher metal density, and to give protection from oxidation (at least for a short time). The measurements were done in transmission mode at 30 K in a vapor flow cryostat using two different silicon monochromators, set for diffraction from (111) planes at Co K edge (7709 eV) and from the (311) planes for Rh K edge (23220 eV). It is worth noticing that the sample is exposed to air for roughly 30 min when positioned on the sample holder and introduced in the cryostat. Both edges were measured with the samples maintained *in situ* at low temperature using the quick monochromator change capability of beamline X1 (less than 15 min to move between the two metal absorption edge energies, including change of detection gas in the ion chambers measuring x-ray intensity). Metal foils were measured simultaneously in the monitor position for accurate calibration of x-ray absorption energies. The EXAFS signal was extracted using the ATHENA program.¹³ Further treatments were performed using classical procedures. For the best data sets, the MINUIT program¹⁴ from CERN was used to refine parameters of the one-shell EXAFS function [see Eq. (2)]:

$$\chi_{\text{fit}}(k) = S_i \sum_j \frac{N_j}{kr_j^2} F_j(k) \cdot \exp^{-2k^2\sigma_j^2} \cdot \exp \frac{-2r_j}{\lambda_j} \cdot \sin[2kr_j + \Phi_{ij}(k)], \quad (2)$$

where S_i is an amplitude scaling factor, F_j is the backscattering amplitude from N_j neighboring atoms of the j th type at a distance r_j from the absorbing atom i , λ_j is the electron mean free path approximated by¹⁵ $[(3.913/k)^4 + k]/0.95$, σ_j is the standard deviation of the interatomic distance, and Φ_{ij} is the

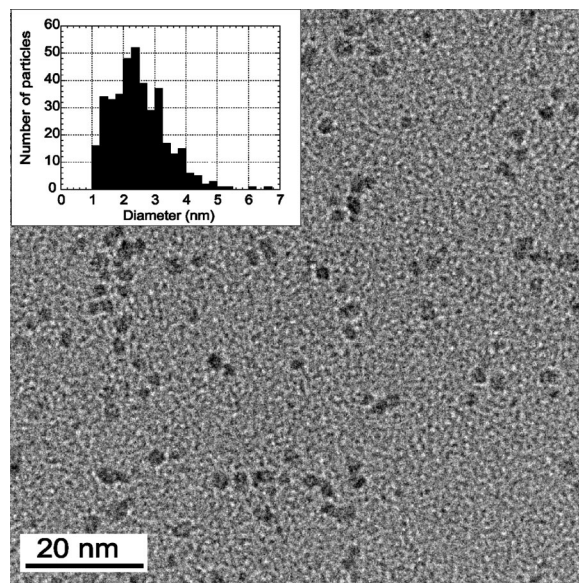


FIG. 1. TEM image of the RT-PVP-Co1Rh3 colloid with size histogram inset.

total phase shift. MacKale functions¹⁶ were also used for F_j and Φ_{ij} . Final values of the refinement are given in Table IV.

III. RESULTS

A. A PVP-CoRh: Structural evolution with temperature

1. Room temperature

Whatever the composition, the particles synthesized in PVP at room temperature (RT-PVP-colloids) look spherical and well dispersed in the polymer matrix when observed by TEM. As for pure cobalt and rhodium particles, the size distribution of the bimetallic particles is narrow. Size histograms, drawn for Co3Rh1, Co1Rh1, and Co1Rh3 colloids, showed a mean size of 2.1, 1.7, and 2.5 nm, respectively, with respective standard deviations of 0.6, 0.4, and 0.9 nm. A TEM image of Co1Rh3 particles with size histogram inset is displayed in Fig. 1. The experimental RDFs of the different RT-PVP colloids are reproduced in Fig. 2 together with the RDFs of pure Co⁵ and pure Rh¹⁷ particles. For each colloid, the coherence length measured from the reduced RDF is shorter than the size measured on TEM images: around 1.4 nm for Co3Rh1, 1.5 nm for Co1Rh1, and 2.0 nm for Co1Rh3. The higher statistics of synchrotron data give more accurate evaluation of the distance for complete damping of oscillations, which is specially difficult for poorly ordered particles. On the measurements performed on the same samples and both instruments, as for Co1Rh1 reported in Fig. 2, very close RDFs were obtained and differences in coherence length were never larger than one period of the last observable oscillation. This leads us to evaluate the uncertainty to 0.2 nm. Apart from the coherence length, an important value taken from the RDF is the position of the first peak which gives the mean metal-metal bond length (d_{mm}). In the absence of fitting with an accurate model, this value remains approximate: here we took the center of the peak at

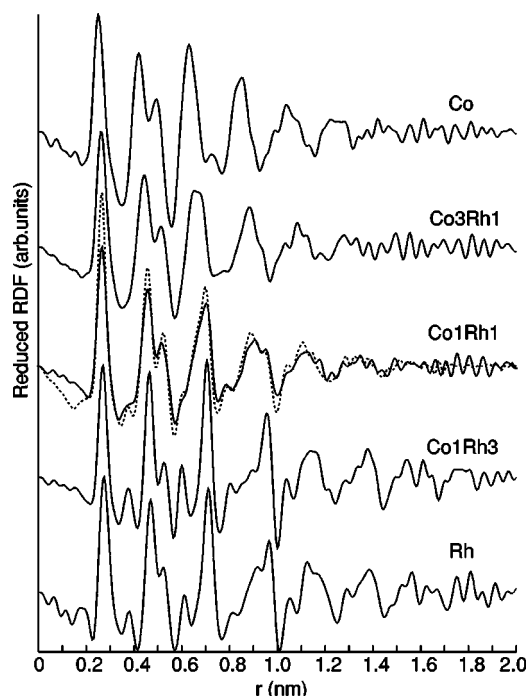


FIG. 2. Experimental WAXS RDF of CoRh particles with different compositions synthesized in PVP at room temperature together with the experimental RDF of pure-cobalt and pure-rhodium particles synthesized in identical conditions. Dashed line: RDF from high energy measurements on ESRF beamline ID15B, for the Co1Rh1 sample.

half maximum and found $d_{mm}=0.263, 0.269,$ and 0.269 nm for Co3Rh1, Co1Rh1, and Co1Rh3, respectively. The error on this measurement can be estimated to less than ± 0.5 pm. The different parameters measured from the TEM and WAXS experiments are summarized in Table I. Clearly, d_{mm} is not proportional to the composition. It increases strongly between pure cobalt and Co3Rh1, then it remains nearly steady from Co1Rh1 to pure rhodium. A comparison of the evolution of the d_{mm} with the composition in the particles and in the bulk, as deduced from the lattice parameters of the bulk phases,¹⁸ is plotted in Fig. 3. In this figure, the plot corresponding to the bulk alloy consists in two different segments according to the structural phases stable at this composition: hexagonal close packed (hcp) below 50.5 at% Rh and face centered cubic (fcc) above. In spite of this structural transition, the first interatomic distance in the alloy (d_{mm}) at room temperature nearly follows a Vegard's law between pure Co (0.250 nm) and pure Rh (0.269 nm). Figure 3 shows

TABLE I. Data extracted from the TEM images and the RDF of the PVP-CoRh colloids synthesized at room temperature.

	Co3Rh1	Co1Rh1	Co1Rh3
Mean diameter (nm)	2.1	1.7	2.5
Standard deviation (nm)	0.6	0.4	0.9
Coherence length (nm)	1.4 ± 0.2	1.5 ± 0.2	2 ± 0.2
d_{mm} (nm ± 0.5 pm)	0.263	0.269	0.269

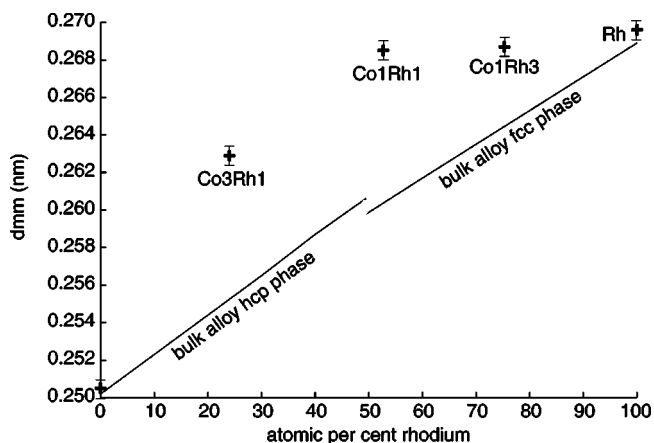


FIG. 3. Comparison between the evolution of d_{mm} in the bulk alloy (solid line) and in the RT-PVP particles (crosses). The discontinuity of the solid line corresponds to the phase transition hcp to fcc in the bulk.

that the d_{mm} evolution in the particles is completely different from the one observed in the bulk alloy.

According to the phase diagram in the bulk alloy, Co3Rh1 crystallizes in the hcp structure. However, the comparison between the experimental RDF of RT-PVP- Co3Rh1 particles and the simulated RDF of a hcp particle of same size and metal-metal distance, clearly shows strong differences, see Fig. 4. In fact, as can be observed in Fig. 2, this experimental RDF displays the same main features as the one of pure RT-PVP-cobalt particles, except for a larger d_{mm} . This particular pattern with broad peaks, a short coherence length and the lack of a specific peak located at the distance $d_{mm}\sqrt{2}$ was identified as the signature of a polytetrahedral atomic organization.⁵ It was, however, impossible to decide in favor of a particular polytetrahedral model, as they all display the

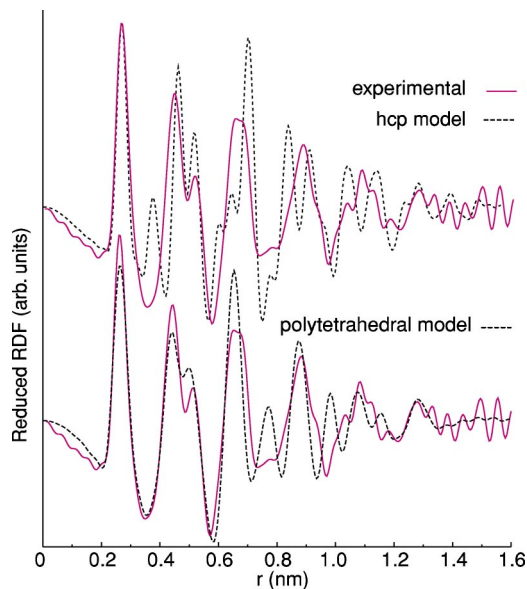


FIG. 4. Comparison between the experimental RDF of RT-PVP-Co3Rh1 and top: a computed RDF of a 129-atom hcp model, bottom: a simulated RDF corresponding to a 105-atom polytetrahedral model with same d_{mm} .

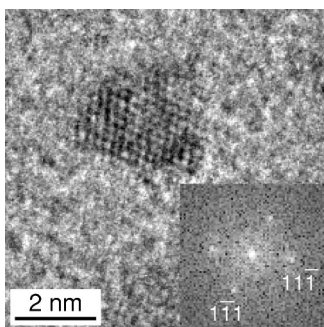


FIG. 5. HRTEM micrograph and corresponding Fourier transform of a fcc RT-PVP-Co1Rh3 particle observed along a [011] zone axis.

same structural features. One of these models, including 105 atoms and having the suitable d_{mm} , was built according to the cluster of clusters approach proposed by Van de Waal.¹⁹ A comparison between the simulated RDF of this model and the experimental RDF of Co3Rh1 is displayed in Fig. 4. Although some differences, particularly in the larger distances, remain, the main features of the experimental RDF are correctly reproduced by the model like the absence of the peak at $d_{\text{mm}}\sqrt{2}$ (near 0.35 nm) observed in the hcp model and more generally in all compact structures. HRTEM investigations of single Co3Rh1 particles do not provide additional structural information as no lattice periodicities were observed.

On the contrary, HRTEM observations of the Co1Rh3 sample clearly reveal lattice fringes in the particles. The analysis of these periodicities agrees with the fcc structure, see Fig. 5. The experimental RDF of this sample has indeed many common features with a fcc structure, particularly in the shorter distances, as can be observed in Fig. 6. The main differences with the 147-atom fcc model, which presents a comparable coherence length, are the sharpness of the peaks and their relative amplitude. Mixing a perfect cuboctahedral

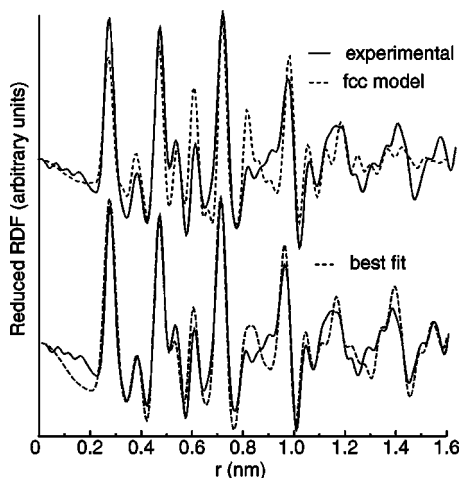


FIG. 6. Comparison between the experimental RDF of RT-PVP-Co1Rh3 particles and top: the computed RDF of a 147-atom perfect fcc cluster, bottom: the computed RDF of a model corresponding to the mixture $\{K_{w1} * 561\text{-atom perfect fcc model} + K_{w2} * 110\text{-atom faulted fcc model}\}$ with $K_{w1}=0.2$ and $K_{w2}=3$.

fcc model with a cuboctahedral fcc model containing an intrinsic stacking fault considerably improves the fit, particularly the amplitudes of the different peaks (see the best fit in Fig. 6). The proportion of the two models in the RDF was adjusted using weighting coefficients K_w . These stacking faults are likely to increase the compacity of the structure and can therefore result from a pure size effect. Besides, two different sizes of particles were required to reproduce more suitably the amplitudes of all the peaks: a 561-atom and a 110-atom models. This can be understood in different ways. First, it can result from a size dispersion. Indeed, the size of the different models, respectively, 2.5 and 1.6 nm, would agree with the TEM results owing to the standard deviation measured in this sample (Table I). However, the respective weight of the models is not consistent with the TEM size histogram. More probably, the need for models with two different sizes results from a progressive loss of coherency with increasing distance due to some structural disorder in the particles.

As observed in Fig. 2, the different peaks get sharper and more numerous with increasing rhodium content. For instance, the peak at $d_{\text{mm}}\sqrt{2}$ just appears in the equiatomic sample Co1Rh1, while the coherence length of this sample remains quite short. This colloid so presents features from both surrounding compositions, i.e., from two completely different models, a nonperiodic polytetrahedral and a periodic fcc models. It is therefore impossible to fit its RDF with a single model. HRTEM observations reveal very few crystallized particles in this sample.

2. Synthesis at 80°C

These samples have been synthesized in conditions similar to the previous ones except for a temperature of 80°C (80°C-PVP colloids). The microanalysis gives Co:Rh compositions close to the initial Co:Rh precursors ratio and TEM investigations show well-dispersed particles with diameters around 2 nm. Therefore, these particles are comparable to the ones synthesized at room temperature. The RDF corresponding to the different samples are reproduced in Fig. 7 together with the RDF of the same samples synthesized at room temperature.

As can be observed, the synthesis temperature only affects the atomic organization in samples with a high rhodium content. Indeed the RDF of 80°C-PVP-Co3Rh1 seems steady. It should be mentioned that this RDF still remains unchanged after annealing of the sample, kept sealed in the capillary, at 120°C during one week. Clearly, the 80°C-PVP-Co1Rh1 sample keeps its coherence length but its pattern is now sharper and closer to a fcc one. Besides its d_{mm} is lower (0.265 nm) than in the RT sample although still higher than expected from the bulk alloy. Enhanced crystallization is also supported by the relative intensities of the main peaks. While the envelope of the RDF for Co3Rh1 and RT-PVP-Co1Rh1 share the same monotonously decreasing shape, the three first peaks in the 80°C-PVP-Co1Rh1 sample are much closer in amplitude which is consistent with an increase of order inside the particles. The RDF of this last sample is in fact very similar to the one of the RT-PVP-Co1Rh3 sample, which means that Co1Rh1 now presents a partially faulted

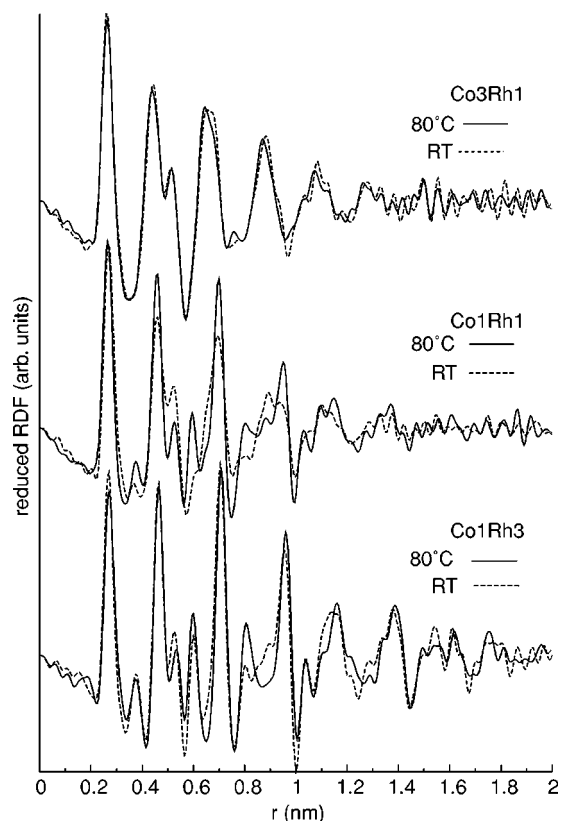


FIG. 7. Evolution of the experimental RDF of the different samples with the synthesis temperature (RT stands for room temperature).

fcc structure. The organization in Co1Rh3 also improves with the temperature and the RDF of the 80°C sample shows sharper peaks, the position and intensity of which agree with a perfect fcc structure. A very good fit, reproduced in Fig. 8, is obtained with a model including two different sizes of fcc cuboctahedral particles: a 561-atom and a 147-atom models, with respective diameters of 2.5 and 1.8 nm. The distance d_{mm} is here equal to 0.266 nm. The data extracted from the WAXS experiments in the high-temperature samples are summarized in Table II.

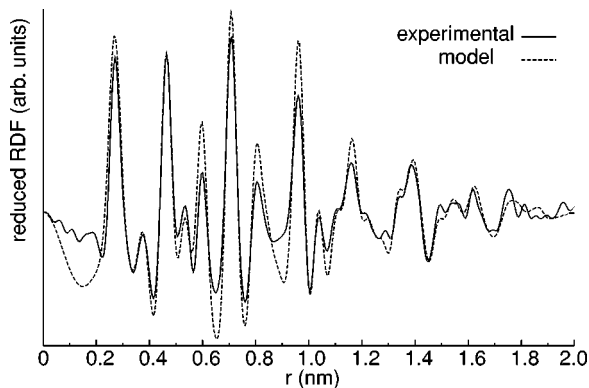


FIG. 8. Comparison between the experimental RDF of 80°C-PVP-Co1Rh3 particles with the computed RDF of a model corresponding to the mixture $\{K_{w1} * 561\text{-atom fcc cuboctahedral model} + K_{w2} * 147\text{-atom fcc cuboctahedral model}\}$ with $K_{w1}=0.1$, $K_{w2}=2$.

TABLE II. Data extracted from the RDF of the 80°C-PVP-CoRh colloids.

	Co3Rh1	Co1Rh1	Co1Rh3
Coherence length (nm)	1.4 ± 0.2	1.4 ± 0.2	1.8 ± 0.2
d_{mm} (nm ± 0.5 pm)	0.263	0.265	0.266

B. HDA-CoRh: Structural evolution with size

The particles synthesized in HDA are much larger, which was the expected effect. They do not adopt a spherical shape, indicating that most of them have coalesced during the growth process. Their size varies between 4.3 and 6.8 nm, with important standard deviations (1.2–2.5 nm).

The particles are formed by several grains as expected from their morphology and they are all fully crystallized. For all the compositions studied, both the fcc and the hcp phases are present, although in different proportions. The results from TEM investigations are gathered in Table III. The Co-rich sample ($\text{Co}_{0.75}\text{Rh}_{0.25}$, i.e., Co3Rh1) presents a large majority of hcp grains, while the Rh-rich sample ($\text{Co}_{0.39}\text{Rh}_{0.61}$) is mainly fcc, although its composition is closer to Co2Rh3 than to Co1Rh3. Finally, the two samples with compositions close to Co1Rh1 ($\text{Co}_{0.53}\text{Rh}_{0.47}$ and $\text{Co}_{0.45}\text{Rh}_{0.55}$) are mainly fcc. However, many regions of these samples exhibit structural distortions, probably due to the presence of numerous faults, which prevents us from unambiguous determination of the structure in as much as one investigated area over four. Figure 9 shows HRTEM images of two particles having different structures, together with their Fourier transforms. The RDF patterns (not shown) are consistent with the structural characteristics determined by HRTEM. For all the compositions, the fit requires a mixture of fcc and hcp models. In the Rh-rich samples ($\text{Co}_{0.45}\text{Rh}_{0.55}$ and $\text{Co}_{0.39}\text{Rh}_{0.61}$) the main structure is clearly fcc, while the RDF of HDA- $\text{Co}_{0.75}\text{Rh}_{0.25}$ is closer to a hcp structure. No evidence for a major structure was obtained in the $\text{Co}_{0.53}\text{Rh}_{0.47}$ sample which presents a broader pattern. The coherence length of these HDA samples are larger than in the PVP samples, but not as large as the diameters measured on TEM images. The d_{mm} bond lengths are shorter than in the PVP samples, but still higher than in the bulk (see Table III).

C. Chemical distribution

The bimetallic character of these particles has been established by different results, in particular the magnetism³ for

TABLE III. HDA-CoRh particles: chemical composition (obtained by microanalysis), particle mean size (ϕ) with standard deviations (σ) and percentage of identified fcc grains deduced from HRTEM investigations. Coherence length (L_{cohe}) and d_{mm} (± 0.5 pm) obtained on the RDFs.

Composition	Size (TEM)		% fcc	L_{cohe} (nm)	d_{mm} (nm)
	ϕ (nm)	σ (nm)			
$\text{Co}_{0.75}\text{Rh}_{0.25}$	6.8	2.5	41	2.4 ± 0.2	0.260
$\text{Co}_{0.53}\text{Rh}_{0.47}$	4.3	1.2	63	2.1 ± 0.2	0.266
$\text{Co}_{0.45}\text{Rh}_{0.55}$	5.6	1.2	58	3.1 ± 0.2	0.265
$\text{Co}_{0.39}\text{Rh}_{0.61}$	5.7	1.5	59	2.1 ± 0.2	0.266

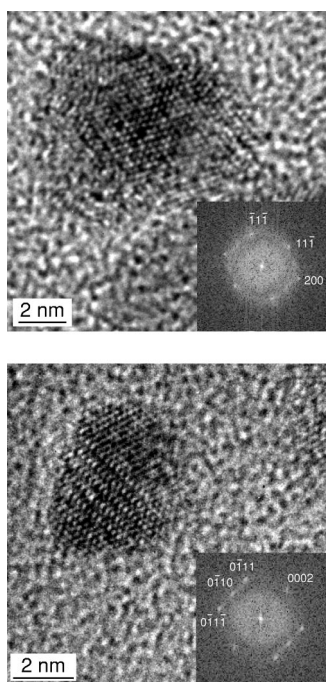


FIG. 9. High-resolution micrographs and Fourier transforms in inset (a) $\text{Co}_{0.39}\text{Rh}_{0.61}$ in HDA, fcc zone axis [011], (b) $\text{Co}_{0.75}\text{Rh}_{0.25}$ in HDA, polycrystalline particle with a hcp structure (bottom left and FT) and a fcc one (top right).

the PVP samples. However, the way the different species organize inside a particle requires the use of element-sensitive techniques. EXAFS experiments have been carried out on the RT-PVP samples, which present the highest size effects. We first worked on the Fourier transforms of the χ function without any phase correction. The modules of these uncorrected Fourier transforms (FT) have been compared either to experimental reference data (Rh foil for instance) or to simulations (see Fig. 10). At the Rh edge, the FT of the Co1Rh3 is very similar to the one obtained on a rhodium foil but with an amplitude twice lower. Both plots show a main peak close to 2.5 nm followed by three much smaller peaks. Let us mention that the same main peak is obtained by modeling the FT corresponding to the first neighbors shell in the rhodium fcc structure. The Co1Rh1 sample (not shown) presents the same main peak but it is associated to a shorter distance, probably a Rh-O bonding. The overall amplitude is lower. In these two samples, the environment of the rhodium atoms looks very close to the one they have in bulk rhodium, in spite of a partial oxidation in the case of Co1Rh1 . For the Co1Rh3 sample, it has been possible to fit the inverse Fourier transform of the main peak using the parameters listed in Table IV. The number of first neighbors has been fixed to 9.9, which is the mean value in particles of about 2 nm.²⁰ The best fit is obtained for rhodium neighbors at a distance close to the one in pure fcc Rh, thus confirming the resemblance with bulk rhodium. XANES analysis of the Co edge reveals partial oxidation of cobalt in this sample. The pre-edge inflexion characteristic of metallic cobalt is suppressed, and the intensity of the white line at the absorption edge is increased, showing a higher mean oxidation state of the cobalt atoms. This is also the case for cobalt in the Co1Rh1

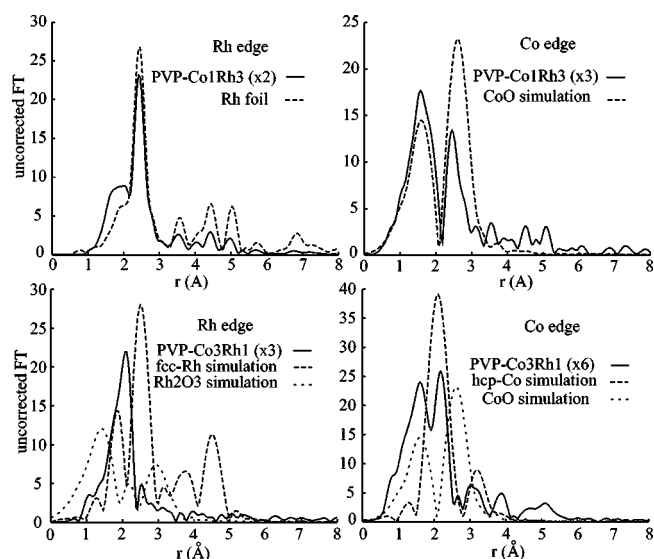


FIG. 10. Uncorrected exafs Fourier transforms modulus of PVP- Co1Rh3 and PVP- Co3Rh1 at the Co and Rh edges, compared with a Rh foil or with simulations.

sample. Indeed, the experimental cobalt K -edge FTs are close to the one calculated with a CoO structure.

The Co-rich particles present a different behavior. At the Rh edge, the uncorrected FT presents a single peak, which is located at a distance too short for a Rh-Rh bond, but too long for a Rh oxide. The same peak is present at the cobalt edge together with an oxide peak. A direct comparison of these FTs with simple models is not sufficient for accurate structure determination. However, fitting attempts at the Rh edge give some indications of the presence of Co in the first neighbors shell.

These different elements, particularly the results obtained on the Rh-rich sample (Rh neighbors around Rh atoms and partial oxidation of cobalt), are consistent with a surface segregation of cobalt atoms. EFTEM experiments are likely to provide a direct proof of such a chemical distribution. However, the PVP particles are very small and the signal of the electron energy loss is too weak to be processed. Only the particles stabilized in HDA can be successfully analyzed. A typical EFTEM analysis of the HDA- $\text{Co}_{0.75}\text{Rh}_{0.25}$ sample is presented in Fig. 11. In the zero-loss image (a), formed by the elastically transmitted electron beam, some contrast already appears in the particle: small dark nuclei are surrounded by light gray areas. Such contrast is not observed in the high-resolution mode which mainly displays a phase con-

TABLE IV. Fitting parameters at the Rh-edge for RT-PVP- Co1Rh3 and for a rhodium foil. Values with * are fixed during the fit (N_{Rh} : number of Rh neighbors, $R_{\text{Rh-Rh}}$: distance, σ^2 : Debye-Waller factor, ΔE_0 : edge shift).

	N_{Rh}	Scaling factor	$R_{\text{Rh-Rh}}$ (Å)	σ^2 (10^{-3}Å^2)	ΔE_0 (eV)	Residual
Co1Rh3	9.9*	0.8*	2.692	7.57	-1.39	0.117
Rh foil	12*	0.83	2.705	4.62	-1.03	0.013

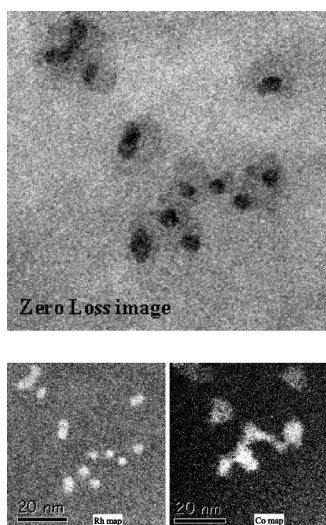


FIG. 11. EFTEM images of HDA- $\text{Co}_{0.75}\text{Rh}_{0.25}$ particles (a) zero-loss image, (b) Rh and Co maps.

trast. The elemental maps obtained by energy filtering on the Rh- $M_{4,5}$ and the Co- $L_{2,3}$ edges show that rhodium atoms concentrate in the nuclei while cobalt atoms spread over much larger zones corresponding to the particles size. Because of the two-dimensional projection in the TEM analyses, we cannot say if cobalt atoms are only located around the rhodium cores or also inside them. In any cases, this result shows without ambiguity the occurrence of a cobalt surface segregation in these particles.

IV. DISCUSSION

We have previously shown that the structure of PVP-CoRh nanoparticles vary from a polytetrahedral arrangement to a structure close to fcc with increasing Rh content. Using a higher temperature during the synthesis (80°C) confirms this behavior. The same polytetrahedral structure is observed in the cobalt-rich particles, at least at this temperature, whereas the structure of the rhodium-rich particles gets closer to perfect fcc. The RDF of the 80°C -PVP-Co1Rh1 samples, which presents the more ambiguous pattern for the room temperature synthesis, evolves towards a pattern characteristic of a partially faulted fcc, i.e., very similar to the one in the RT-PVP-Co1Rh3 sample. This is an indication of the low stability of the polytetrahedral structure at this composition. The structural evolution of the Co1Rh1 and Co1Rh3 particles with the temperature is accompanied by a slight decrease of the first metal-metal bond length (d_{mm}). Increasing the size of the particles also affects their structural behavior. The big cobalt-rich HDA particles mainly display a hcp structure, like in the bulk alloy, even if some fcc particles are observed. For the Co3Rh1 composition, the critical size, above which the bulk structure (hcp) becomes more stable than the polytetrahedral one, thus lies between 2 and 6 nm. Whatever the size, the Rh-rich particles always crystallize in the fcc structure of the bulk alloy. However, the bigger ones also present some hcp regions. The case of the equiatomic composition is again more complex. As for the

other compositions, the bigger particles present both fcc and hcp areas. However, none of these structures is particularly favored, which agrees with the occurrence of the hcp to fcc phase transition at this composition in the bulk alloy. It is worth recalling that the study of the structural evolution with size has required a change in stabilizer, i.e., the use of the HDA ligand instead of the PVP polymer. We are thus not able to distinguish between a pure size effect and a combined size and environment effect.

The particular evolution of the d_{mm} in the RT-PVP-CoRh samples has also been pointed out. Synthesis at higher temperatures as synthesis in other media do not change drastically this particular evolution. In other words, the first metal-metal bond length remains in all the studied samples, higher than in the bulk alloy with same composition. In particular, for samples with at least 50 at% Rh, the d_{mm} comes very close to the one in pure Rh particles (same as in bulk Rh). As the core-atoms are involved in more bondings than the surface atoms, this feature could be attributed to a Rh-rich core. Surface segregation in binary alloys is driven by different forces: the difference between the surface energies of the involved elements, their size difference, and their ability (inability) to mix in the bulk (tendency to phase separation or to order). Cobalt has a slightly lower surface energy than rhodium²¹ so that, at any composition, the system will lower its surface energy if cobalt comes to the surface. Rhodium having a larger atomic radius than cobalt, the elastic strain energy will be lower when Rh lies at the surface in Co-rich alloys. Finally, the CoRh alloy forms a solid solution all over the phase diagram, so that the heteroatomic bond driving force will not have an important effect on the segregation of this alloy. Ellison *et al.*²² carried out an experimental study of the segregation in macroscopic specimens of CoRh and showed some surface segregation of the solute element. According to their results, the driving force of the segregation would depend on the composition: surface energy in Co-rich samples and atomic size in Rh-rich ones. In conclusion, some cobalt surface segregation can be expected in the Rh-rich particles while the chemical distribution in the Co-rich particles remains difficult to foresee because of the competition between the surface energy and the atomic size driving forces. Our investigations by EFTEM clearly showed a surface segregation of cobalt in Co-rich HDA particles. However, contrary to the PVP polymer which has nearly no interactions with the particles, the HDA ligand can have more affinities with the cobalt atoms and thus play a role in the observed segregation. Therefore, the direct use of this result to conclude on the chemical distribution in the PVP-CoRh particles remains questionable. For these small particles, EXAFS experiments have given different clues for the presence of a Rh-rich core. Indeed, in the Rh-rich particles, our results show that the rhodium atoms have mainly the same environment as in bulk rhodium and reveal the presence of oxide at the cobalt edge. The chemical distribution in the Co-rich sample is not so clear although evidence for oxidation, only at the cobalt edge, would also agree with cobalt surface segregation. The overall difficulty to prevent the samples from any oxidation and though to extract reliable information from these experiments prevents us from further analysis in most of the samples. Finally, the link between the

value of the metal-metal bond length and the chemical distribution in the particles is probably not as straightforward as mentioned previously. Indeed, the slight decrease of the d_{mm} in the Rh-rich 80°C samples could be interpreted as the result of some intermixing of the chemical species instead of a core-shell distribution. However, this decrease is accompanied by an increase of the crystallographic order in these samples. For comparison, room temperature Rh-rich HDAsamples which are fully crystallized in compact structures (mainly fcc) also present a lower d_{mm} . Besides, the Co-rich HDA samples, which also crystallize in compact structures, present both characteristics: a lower d_{mm} and a rhodium core, as evidenced by EFTEM. The difference between the respective weights of Rh-Rh, Rh-Co, and Co-Co contributions to scattering probably also contribute to the overall increase of the d_{mm} measured by WAXS compared to the one expected from the bulk.

The experimental techniques implemented in this study reach their limits in these ultrafine particles. In order to bring more information on these samples and more specifically on the cobalt-rich ones, molecular dynamics and Monte-Carlo calculations using a n -body semiempirical interaction model for the particles are now in progress. In any case, if not definitely proved for the different compositions, all our experimental results agree with a cobalt segregation at the surface, which should play an important part in the magnetic behavior of these particles.

V. CONCLUSION

In this paper, we have completed the structural and chemical study of CoRh nanoparticles synthesized in mild conditions using a wide range of experimental techniques. We

have shown that the structure of the small particles (2 nm) evolves from a polytetrahedral arrangement in Co-rich particles to a faulted fcc structure in Rh-rich ones. Using a higher temperature during the synthesis does not affect the polytetrahedral arrangement in the Co-rich particles but increases the crystallographic order in the Rh-rich ones. Increasing the size of the particles allowed us to stabilize the bulk phases, with a majority of hcp in the cobalt rich side, and fcc in the Rh-rich one, in particles 4–6 nm large. In all the studied particles, the first metal-metal bond length proves larger than in the bulk alloy of same composition. Moreover, introduction of a small amount of rhodium in the particles induces a larger shift towards the mean bond length in pure rhodium than expected from a Vegard's law. This particular behavior can be explained by the occurrence of both some surface disorder and cobalt segregation. Evidence for this surface segregation has indeed been given by element-sensitive techniques on some of the samples, if not all. In particular, some ambiguity remains concerning the smaller cobalt-rich samples. Complementary information should soon be brought by calculations using a n -body semiempirical interaction model, now in progress.

ACKNOWLEDGMENTS

The authors acknowledge the European Synchrotron Radiation Facility for provision of synchrotron radiation facilities and we would like to thank Dr. V. Honkimaki for assistance in using beamline ID15B. They also acknowledge financial support through the IHP-Contract No. HPRI-CT-1999-00040/2001-00140 of the European Commission for the measurements on beamline X1 at Hasylab, and the assistance of Dr. P. Kappen and Dr. J. Wienold in using this beamline.

*Author to whom correspondence should be addressed. Electronic address: casanove@cemes.fr

¹A. J. Cox, J. G. Louderback, S. E. Apsel, and L. A. Bloomfield, *Phys. Rev. B* **49**, 12295 (1994).

²P. Villasenor-Gonzalez, J. Dorantes-Davila, H. Dreyssé, and G. M. Pastor, *Phys. Rev. B* **55**, 15084 (1997).

³D. Zitoun, M. Respaud, M.-C. Fromen, M.-J. Casanove, P. Lecante, C. Amiens, and B. Chaudret, *Phys. Rev. Lett.* **89**, 037203 (2002).

⁴J. Osuna, D. de Caro, C. Amiens, B. Chaudret, E. Snoeck, M. Respaud, J.-M. Broto, and A. Fert, *J. Phys. Chem.* **100**, 14571 (1996).

⁵F. Dassenoy, M.-J. Casanove, P. Lecante, M. Verelst, E. Snoeck, A. Mosset, T. O. Ely, C. Amiens, and B. Chaudret, *J. Chem. Phys.* **112**, 8137 (2000).

⁶G. Moraitis, H. Dreyssé, and M. A. Khan, *Phys. Rev. B* **54**, 7140 (1996).

⁷M.-C. Fromen, A. Serres, D. Zitoun, M. Respaud, C. Amiens, B. Chaudret, P. Lecante, and M.-J. Casanove, *J. Magn. Magn. Mater.* **242**, 610 (2002).

⁸D. Zitoun, C. Amiens, B. Chaudret, M.-C. Fromen, P. Lecante, M.-J. Casanove, and M. Respaud, *J. Phys. Chem.* **107**, 6997 (2003).

⁹T. O. Ely, C. Pan, C. Amiens, B. Chaudret, F. Dassenoy, P.

Lecante, M.-J. Casanove, A. Mosset, M. Respaud, and J.-M. Broto, *J. Phys. Chem.* **100**, 695 (2000).

¹⁰D. Zitoun, Ph.D. thesis, Université Paul Sabatier, Toulouse, France, 2003.

¹¹P. Bayle-Guillemaud, A. Barbier, and C. Mocuta, *Ultramicroscopy* **88**, 99 (2001).

¹²F. Dassenoy, M.-J. Casanove, P. Lecante, C. Pan, K. Philippot, C. Amiens, and B. Chaudret, *Phys. Rev. B* **63**, 235407 (2001).

¹³M. Newville, *J. Synchrotron Radiat.* **8**, 322 (2001).

¹⁴F. James and M. Roos, MINUIT, 1976, CERN Computing Center. Program Library. CERN/DD internal report 75/20.

¹⁵*EXAFS: Basic Principles and Data Analysis*, edited by B. K. Teo (Springer-Verlag, New York, 1986).

¹⁶G. McKale, B. W. Veal, A. P. Paulikas, S. K. Chan, and G. S. Knapp, *J. Am. Chem. Soc.* **110**, 3763 (1988).

¹⁷C. Pan, E. Ramirez, K. Philippot, and B. Chaudret (unpublished).

¹⁸W. Koster and E. Horn, *Z. Metallkd.* **43**, 444 (1952).

¹⁹B. W. V. de Waal, *J. Non-Cryst. Solids* **189**, 118 (1995).

²⁰R. E. Benfield, *J. Chem. Soc., Faraday Trans.* **88**, 1107 (1992).

²¹L. Z. Mezey and J. Giber, *Jpn. J. Appl. Phys., Part 1* **21**, 1569 (1982).

²²K. A. Ellison, P. R. Underhill, and W. W. Smeltzer, *Surf. Sci.* **182**, 69 (1987).